Experimental Thermal and Fluid Science 172 (2026) 111665

Contents lists available at ScienceDirect

Experimental Thermal and Fluid Science

journal homepage: www.elsevier.com/locate/etfs

Experimental investigation of turbulence in non-Newtonian fluids using ultrasound velocity profiling

B.K. Yusufi *, Z. Kapelan [1], D. Mehta [1]

Section Sanitary Engineering, Department of Water Management, Faculty of Civil Engineering, Delft University of Technology, Delft, 2628 CN, The Netherlands

ARTICLE INFO

Keywords:
Non-Newtonian fluids
Turbulent pipe flow
Ultrasound velocity profiling (UVP)
Rheology
Turbulence modeling
Slurry Flow

ABSTRACT

Transportation of non-Newtonian fluids (NNFs) through pipelines is a cornerstone of modern infrastructure. While the laminar and transitional flows have been extensively studied, the turbulent behavior of NNFs remains poorly understood. This study investigates large-scale pipe-loop experiments on clay–water slurries, spanning Reynolds numbers $\approx 1.1\times10^4$–1.75×10^5 in a 100-mm diameter facility. Using non-invasive ultrasound velocity profiling (UVP) together with wall shear stress measurements, we characterize flows ranging from weakly to highly non-Newtonian conditions with concentrations up to 19%(w/w). The experiments show that the transition to the log-law region is delayed and the log-law intercept shifts upward with increasing concentration, reflecting the redistribution of stresses as shear-thinning and yield effects become more pronounced. To further interpret these findings, the experimental observations were compared with established modeling approaches. Semi-empirical correlations exhibited intermediate performance (mean absolute error, MAE, up to 0.55 Pa for wall shear stress and 0.15 m/s for velocity), while the Launder–Spalding wall function performed worst due to its assumption of constant viscosity (MAE ≈ 1.48 Pa and 0.08 m/s). In contrast, the rheology-based wall function achieved the most reliable predictions, with minimal deviations from experiments (MAE ≈ 0.20 Pa for wall shear stress and 0.06 m/s for velocity). Overall, this work provides a comprehensive experimental and modeling assessment of turbulent non-Newtonian pipe flow at an industrial scale, yielding new insights into flow physics and establishing a valuable reference for future experimental and computational studies.

1. Introduction

Non-Newtonian fluids (NNFs) are generally encountered in various industrial and engineering applications, including chemical processing, petroleum extraction, mining, deep-sea mineral recovery, marine dredging, sediment transport, and wastewater management [1]. Industrially relevant flows are typically highly turbulent, primarily due to the large pipe diameters involved and the necessity of maintaining sufficiently high operating velocities to prevent particle settling and pipeline clogging [2]. While the term ‘non-Newtonian’ encompasses complex behavior including viscoelasticity and thixotropy, this study solely focuses on shear-thinning, time-independent fluids, where viscosity is a function of shear rate only. Accordingly, throughout this article, the abbreviation NNFs refers to purely viscous, time-independent shear-thinning fluids, unless stated otherwise.

The turbulent flow of NNFs has historically been modeled by extending Newtonian-based laws and equations, with modifications for shear thinning and viscoplasticity. This led to the development of several semi-empirical models that include corrections to the classical Newtonian logarithmic law of the wall or Nikuradse friction factor correlations. For instance, Dodge and Metzner [3] employed dimensional analysis to propose friction factor and velocity profile correlations; similarly, Torrance [4] introduced viscosity-dependent corrections to the von Kármán constant in the mixing length model. Further, Wilson and Thomas [5], Slatter [6] formulated turbulence models based on micro-eddy formation dynamics and effective particle roughness, respectively.

Despite their widespread use, these semi-empirical correlations exhibit significant discrepancies when applied at industrial scales or conditions deviating from the specific experimental environments in which they were trained [7,8]. These discrepancies have been attributed to various factors, including limited training datasets, oversimplified turbulence assumptions, or the presence of wall slip in viscoplastic and shear-thinning fluids. For example, Particle Image Velocimetry (PIV) measurements show that slip inflates rheological parameters [9], and

* Corresponding author.
E-mail addresses: b.k.yusufi@tudelft.nl (B.K. Yusufi), Z.Kapelan@tudelft.nl (Z. Kapelan), D.Mehta@tudelft.nl (D. Mehta).
[1] Contributing authors.

https://doi.org/10.1016/j.expthermflusci.2025.111665
Received 15 May 2025; Received in revised form 31 October 2025; Accepted 23 November 2025
Available online 24 November 2025

rheometry without slip correction misrepresents wall-shear rates and yield stresses [10]. Various comparative studies [1,11–15] have further demonstrated that these models often fail to generalize across different flow regimes, resulting in substantial deviations from experiments. In fact, Heywood and Cheng [16] found that wall shear stress estimations from these semi-empirical correlations could deviate by as much as ±50% from experimental measurements under turbulent conditions.

Computational fluid dynamics (CFD) approaches, such as the Reynolds-Averaged Navier–Stokes (RANS) method, incorporate modifications including modified damping functions [17,18], second-moment closures [19], and energy redistribution mechanisms [20,21]. The integration of these closures has significantly improved turbulence predictions, highlighting the importance of non-Newtonian contributions to momentum and transport equations (see Amani et al. [22] for detailed discussion). However, these models involve complex mathematical formulations with underlying assumptions such as linear coupling between viscosity fluctuations and strain rates, neglecting higher-order nonlinear terms, and the assumption of isotropic turbulence. Additionally, they often rely on default Newtonian-based constants, which may not accurately represent the behavior of NNFs. Further, the computational expense associated with these advanced closures restricts their practical application to flows in the early stages of turbulence. Readers are encouraged to refer to the recent review by Yusufi et al. [23], where these aspects are discussed in detail.

Experimental studies that could contribute to the development of turbulence models for NNFs remain limited. Classical investigations by Metzner and Reed [24], Dodge and Metzner [3], and Slatter [6] provided some insights; however, these studies primarily focused on wall shear stress measurements, without detailed characterization of local turbulence properties. While non-conventional imaging techniques, such as X-ray and MRI-based velocimetry, are constrained by low spatial resolution, operational complexity, high costs, and radiation exposure, rendering them impractical for large-scale industrial applications [25]. Conventional optical methods, including PIV and Laser Doppler Velocimetry (LDV), offer improved spatial resolution; however, experimental investigations on non-Newtonian turbulence remain scarce. The work of Güzel et al. [26] and, more recently, Charles et al. [27] has provided insights into non-Newtonian flow characteristics in pipe flow, though these studies have primarily been conducted under the transitional regime.

Only a handful of experimental studies have focused on the fully developed turbulent flow of NNFs. Early investigations by Park et al. [28], Escudier and Presti [29], and Peixinho et al. [30] suggest that velocity profiles in non-Newtonian turbulent flows adhere to the 1/7th power law with a log-law shift. As the Reynolds number increases, this shift is expected to diminish, converging toward predictions from classical Newtonian correlations such as those of Blasius [31], Colebrook [32]. While axial velocity fluctuations between Newtonian and NNFs exhibit similar trends, significant deviations are observed in tangential and radial velocity fluctuations [33]. More recently, Mitishita et al. [34] investigated shear-thinning Carbopol solutions using LDV in a rectangular duct, showing that yield stress enhances turbulence anisotropy by increasing streamwise fluctuations and reducing wall-normal components.

Additionally, García-Blanco et al. [35] demonstrated that in abrupt contraction flows of viscoplastic fluids, pressure losses deviate from analytical and numerical predictions due to yield stress and shear-thinning effects. Recent studies further broaden the context: Shi et al. [36] reported modifications to mean velocity profiles in turbulent pipe flow of viscoelastic polymer solutions, while Breakey et al. [37] provided PIV/PTV data on particle-laden turbulent vertical pipe flows at high Reynolds numbers. While these studies broaden our understanding of complex fluids, their emphasis on viscoelastic and multiphase systems places them beyond the scope of the present study, which is limited to shear-thinning and viscoplastic single-phase flows.

Despite these advancements, the existing experimental literature on turbulent NNFs faces two key challenges: (1) scaling to industrially relevant conditions, and (2) limitations of optical measurement techniques. While optical methods, such as PIV and LDV, offer high spatial resolution, they are restricted to transparent fluids and dilute suspensions, making them impractical for concentrated and opaque industrial flows [38]. Acoustic-based techniques have therefore emerged as promising alternatives. Doppler-based methods, such as Ultrasound Velocity Profiling [39], and correlation-based techniques like echo-PIV, enable velocity measurements in opaque fluids where optical methods fail [40]. These methods open new possibilities for studying turbulent NNF flows under realistic conditions [41]. Nevertheless, the lack of high-turbulence experimental data, combined with discrepancies in existing numerical models, underscores the absence of a robust predictive framework for highly turbulent non-Newtonian flows. As a result, Newtonian-based turbulence models are often employed, despite their inherent limitations [21].

The objective of this study is twofold. First, we experimentally investigate the turbulent flow of NNFs using Ultrasound Velocity Profiling (UVP), a non-intrusive technique that measures the Doppler shift of reflected ultrasound signals from moving particles. Over the years, UVP has been widely used in multiphase flow research, with applications ranging from in-line rheometry [42–46], concentration profiling [47,48], flow rate analysis [49–52], and medical diagnostics [53]. However, only a handful of studies have explored the turbulent flow of NNFs in pipes using UVP [54–56]. While these studies have demonstrated the feasibility of UVP in resolving complex flow dynamics, comprehensive large-scale investigations spanning a wider spectrum of fluid properties and turbulence scales remain scarce. To address this, we experimentally examine the turbulent mean velocity profiles of a homogeneous non-Newtonian clay-water slurry across concentrations (1.5%–19% w/w) and Reynolds numbers ($\approx 1.1 \times 10^4$–1.75×10^5). This analysis evaluates the accuracy and reliability of UVP for characterizing highly turbulent non-Newtonian flows over an extended range of operating conditions.

Second, we assess the predictive capability of existing models for wall shear stress and mean velocity through a comparative analysis. We contrast the experimental measurements with three classes of numerical approaches: (i) the most commonly used standard wall function [57], to test whether Newtonian-based correlations remain adequate at high turbulence; (ii) a rheology-based wall function that incorporates non-Newtonian viscosity, as developed in [58,59]; and (iii) the classical Dodge–Metzner velocity and friction-factor correlations [3]. This will help better understand the applicability and limitations of these turbulent non-Newtonian flow models and provide a benchmark for our experimental measurements.

The paper is structured as follows. Section 1 provides the background and motivation; Section 2 details the experimental setup and slurry characterization; Section 3 describes the computational and semi-empirical models used for comparison. Section 4 presents the discussion of experimental results and comparisons with the numerical models, and Section 5 concludes with the key findings and future outlook.

2. Experiments

2.1. Flow loop

Measurements are performed on a closed-loop recirculation PVC pipeline system (referred to here as Beta-loop) that spans 225 m and has an internal diameter of 100 mm. The experimental setup, depicted schematically in Fig. 1, includes horizontal, vertical, and 2° inclined sections, with the horizontal section considered for investigation. A variable-frequency centrifugal slurry pump (NT 3153, Xylem) was used to maintain the slurry flow, with the desired flow rate achieved by adjusting the outlet pressure or the pump rotor speed (in Hz). The system is equipped with a slurry tank with a capacity of approximately

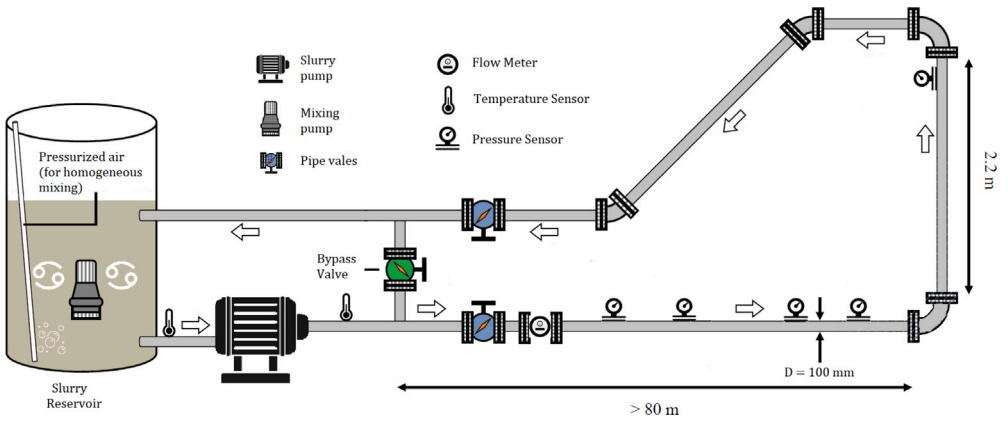

Fig. 1. Schematic representation of the experimental test facility (Beta-Loop) located at Deltares, Delft, Netherlands.

Table 1
A Summary of the initial conditions of the experiments.

Cases -	Flow rates (l/s)	Avg velocities (m/s)	Reynolds no* $Re_w \times 10^3$
Q1	7.93	1.04	11–71
Q2	9.66	1.23	15–86
Q3	13.01	1.66	24–116
Q4	16.73	2.13	26–149
Q5	19.25	2.53	45–175

* Reported Reynolds numbers (Re_w) are expressed as ranges to reflect variations with slurry concentration and rheological properties.

4 m^3 with a total volume (including the pipes) of approximately 5.7 m^3 used to hold the slurry during the measurements. To further enhance the mixing process, an additional mixing pump is installed inside the tank.

The experimental procedure followed a systematic approach, ensuring consistency across the different phases of the study. Before starting any measurement, the slurry was circulated for approximately 30 min to ensure fully homogeneous conditions. Pressure drop across the test section was measured using three pressure transducers (PDCR5031, GE) located along the pipe at 64.6 m, 39 m, and 14.6 m, respectively, from the pipe bend. These transducers measured absolute pressure with a micro-machined silicon piezoelectric resistive sensor, providing a linear output voltage proportional to the measured pressure. The sensors offer high accuracy within ±2% over a 0-6 bar range. The wall shear stress for each stage was calculated from the pressure drop using the following equation, where L is the distance between the pressure transducers, and D is the diameter of the pipe.

$$\tau_w = \frac{D \cdot \Delta P}{4L} \tag{1}$$

The slurry temperature, monitored using a high-accuracy temperature sensor (STS-PT100, Ametek; 0.04% accuracy), ranged from 14.01 °C to 16.63 °C, with an average of 15.41 °C. Identical conditions were maintained for rheology measurements in the rheometer. The average volumetric flow rate is determined by an electromagnetic flow meter (Optiflux 2300C, Krohne), located approximately 10 m downstream of the slurry tank and 40 m upstream from the test section. This flow meter is well-suited for measuring flow in slurries and wastewater, with a maximum error of ±5%. To ensure consistent readings and minimize the impact of incidental fluctuations and spikes, the pressure, temperature, and flow meter readings were averaged over a 30-second period, with 3000 data points collected at a sampling interval of 10 ms. To achieve a range of flow rates, the pump speed was varied between 15 Hz and 32 Hz in a ramp-up sequence, resulting in flow velocities ranging from 1 m/s to 2.5 m/s, thereby generating highly turbulent flow conditions, as outlined in Table 1.

2.2. Ultrasonic velocity profiling

We used Doppler-based ultrasonic Velocity Profiling (UVP), which measures the change in the ultrasonic (US) pulse as it is reflected by moving particles, providing the velocity component along the beam direction [39]. The system operates using a transducer that both emits and receives ultrasonic pulses. Initially, it emits short bursts of sinusoidal ultrasonic waves along the beam axis, subsequently switching to a listening mode to receive the reflected signals, as illustrated in Fig. 2.

The velocity profiles were measured using the Met-Flow 5th-generation UVP-DUO profiler, integrated with Met-Flow software version 4.1 for data processing and analysis. The test section was positioned more than 50 m downstream from the inlet and 10 m upstream from the pipe bend, ensuring both entry and exit length requirements were met (see Durst et al. [60]). We used standard 4 MHz transducers, which were non-invasively affixed to the pipe using custom-made, 3D-printed mounts positioned at a Doppler angle of 70° (20° from the vertical). To ensure effective acoustic coupling and eliminate air gaps, an ultrasound coupling gel was applied between the transducer and the pipe wall.

The measurement process began by detecting strong echoes from the fixed pipe walls, which were used as a reference for signal calibration. The separation between these echoes corresponds to the pipe's internal diameter and thus provides a baseline for resolving particle-induced signals in the fluid. After wall detection, the UVP parameters (summarized in Table 2) were systematically adjusted according to the increasing pipe flow rates and slurry concentrations.

Higher flow rates required an increase in the pulse repetition frequency (PRF) to capture larger Doppler shifts, which consequently reduced the measurable depth. Conversely, higher slurry concentrations necessitated greater ultrasound voltage and receiver gain to maintain signal quality. Nevertheless, for all the test cases, at least half of the pipe diameter was still covered within the effective measurement range. The measurement duration was fixed at five minutes, chosen as a conservative interval ensuring stable and time-converged velocity profiles for each test case.

2.3. Slurry characteristics

The slurry used in this study consists of kaolin clay-water mixtures, a fine, white, powdered clay commonly employed in ceramics [61]. Five different concentrations were prepared by adding clay powder to the beta-loop tank and circulating the mixture with the main pump at 30 Hz for ~ 30 min to ensure thorough mixing. An auxiliary mixer in the tank prevented particle settling. After mixing, representative slurry samples were collected from a wall-mounted tapping port located on the inner curvature of the bottom horizontal section, immediately

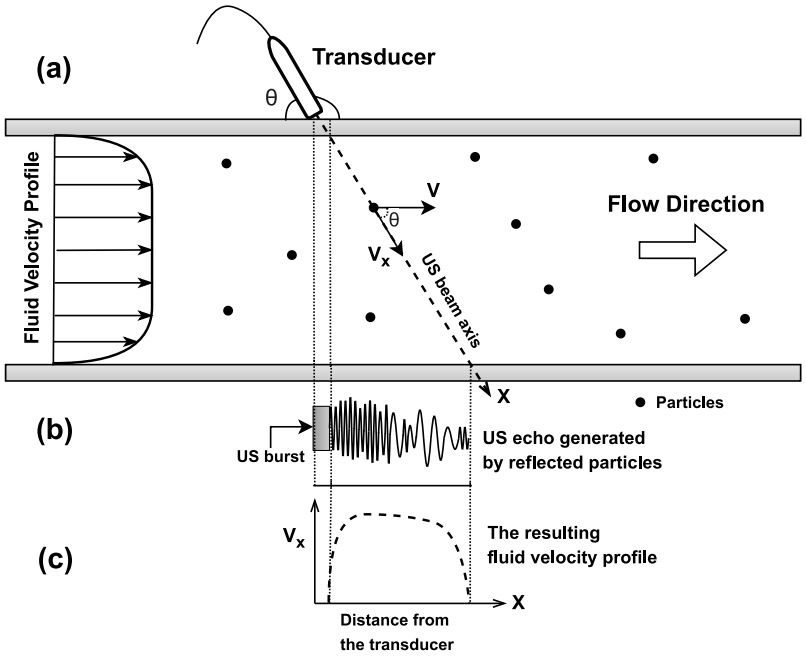

Fig. 2. Schematic of the UVP principle. (a) Measurement system. (b) Ultrasonic echo signal. (c) Measured velocity distribution.

Table 2
Experimental UVP parameters.

Parameter	Value	Parameter	Value
Ultrasound frequency	4 MHz	Pulse cycles	2
Bursts per profile	128, 256	Measurement time	5 min
Time resolution	28–106 ms	Sampling rate	9.4–35.7 Hz
Profiles per flow rate	3,000–10,800	Sound velocity	1480–1493.8 m/s
Transducer angle	20° (from vertical)	Channel width	0.37 mm
Velocity resolution	13–26 mm/s	Recorded channels	144–305

Table 3
Slurry characteristic.

Slurry	Conc %(w/w)	Density (kg/m^3)	Speed of sound (m/s)
S1	1.5	1009	1484.06
S2	5.4	1032	1486.11
S3	8.5	1052	1487.83
S4	13.8	1087	1490.81
S5	19.0	1124	1493.78

upstream of the 90° bend leading to the vertical riser and subsequently used for rheology, particle size distribution, and flow experiments.

The measured slurry densities, determined via pycnometer, ranged from 1.009 to 1.124 g cm^{-3}, with the dry clay powder having a specific gravity of 2.395. Clay concentrations were determined using the dry oven method, while the particle-size distribution was analyzed with a Microtrac Bluewave diffraction analyzer, yielding a range of 1 to 55 μm with a median diameter (D_{50}) of 6 μm. The speed of sound in the slurries, a key input for the UVP measurements, was computed following de Korte and Brouwers [62]. These properties, along with other key characteristics, are summarized in Table 3.

2.4. Rheometry

Past investigations have shown that the clay-water mixture can be described as the two-parameter power law (PL) model at lower concentrations and the three-parameter Herschel–Bulkley (HB) model at higher concentrations [63]. While PL follows a shear thinning behavior, HB fluids have distinct yield and post-yield behavior and behave non-linearly as shear thinning when the local shear exceeds the yield stress [64]. Fig. 3 shows a typical representation of PL and HB fluids on a shear stress-shear rate plot (called a rheogram) compared to Newtonian and Bingham-plastic (BP) fluids.

The expression for HB fluids was proposed by Herschel and Bulkley [65] typically given by the following equation, where τ_y represents the yield stress, m is the consistency index and n is the behavior index:

$$\tau = \tau_y + m\dot{\gamma}^n \tag{2}$$

Eq. (2) is applicable when the magnitude of the stress ($|\tau|$ or τ) is greater than or equal to the yield stress (τ_y), typically: $|\tau| \geq \tau_y$. When $|\tau| < \tau_y$, the shear rate ($\dot{\gamma}$) is equal to 0. Also, this equation can be treated as a generalized equation for all purely viscous time-independent NNFs and reverts back to BP fluid for $n = 1$, PL fluid for $\tau_y = 0$, and Newtonian fluid for $\tau_y = 0$, $n = 1$ and $m = \mu$.

However, for the HB model (where $n < 1$), a key limitation arises because as $\dot{\gamma} \to \infty$ the apparent viscosity (η) tends to zero ($\tau/\dot{\gamma} \sim m\dot{\gamma}^{n-1} \to 0$). This non-physical behavior implies that the suspension viscosity falls below that of the carrier fluid, an artefact documented for sewage and digested sludges [66,67], and in turbulent pipe–flow studies where HB grossly overpredicts the generalized Reynolds number at high shear rates [33,68].

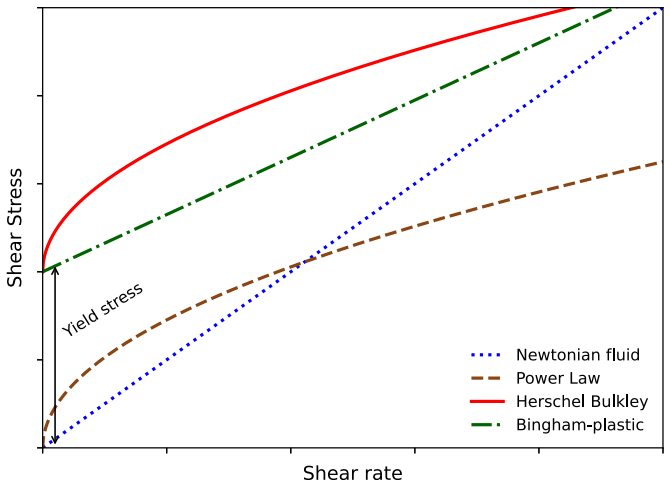

Fig. 3. Types of time-independent flow behavior.

To avoid this, several authors introduce a finite high–shear plateau viscosity μ_∞ (typically close to the solvent viscosity), such that $\lim_{\dot\gamma\to\infty}\eta = \mu_\infty$ [69,70]. The resulting Combined Herschel–Bulkley (CHB) model is written as

$$\tau(\dot\gamma) = \tau_y + \mu_\infty\dot\gamma + m\dot\gamma^{\,n} \tag{3}$$

which preserves HB behavior at low shear rates while enforcing a bounded viscosity at high $\dot\gamma$ (see Thota Radhakrishnan et al. [71]). Notably, the CHB model reduces to the well-known Sisko model [72,73] when $\tau_y = 0$:

$$\tau(\dot\gamma) = \mu_\infty\dot\gamma + m\dot\gamma^{\,n} \tag{4}$$

In the present study, the flow rates and therefore the wall shear stresses were extremely high, with $\tau_{\max} \approx 12$ Pa corresponding to $\dot\gamma \approx 30{,}000\ \mathrm{s}^{-1}$. As shown in Fig. 4, under these conditions, the classical PL and HB models yield apparent wall viscosities η_w that fall unrealistically below the carrier fluid viscosity. By contrast, the Sisko and CHB formulations enforce the physically consistent asymptote $\eta_w \to \mu_\infty$ at large $\dot\gamma$, while retaining the standard PL/HB behavior at low shear.

The rheological characterization of the slurry was carried out using a rotational rheometer (MCR302, Anton Paar) equipped with a standard concentric cup–bob geometry (cup diameter: 29.29 mm, bob diameter: 27 mm, bob length: 40.5 mm). Since rheological properties are temperature-dependent, a Peltier temperature control system maintained the setpoint within ±0.1 °C. The concentration and temperature of the slurry samples matched those in the Beta-loop. Pre-shear was applied at 1000 s^{-1} for 5 min, followed by a 5 min rest to erase material memory before measurements [74]. Each rheogram was then obtained by applying a logarithmically spaced shear-rate sweep from 0.1 to 1000 s^{-1}, producing approximately 300 points with steady shear stress recorded at each step. To ensure reliability, data were truncated at the onset of secondary flows in the cup–bob geometry, consistent with the criteria discussed in Thota Radhakrishnan [75].

The measured shear stress–shear rate data were fitted to three constitutive models: (i) Newtonian at very low concentrations (Slurry S1); (ii) the Sisko model (Eq. (4)) for moderate concentrations (Slurries S2–S3); and (iii) the CHB model (Eq. (3)) for higher concentrations (Slurries S4–S5). In the non-Newtonian cases, the high-shear viscosity μ_∞ was constrained to the carrier-fluid viscosity (water), i.e. $\mu_\infty = 1.0\times10^{-3}$ Pa s, ensuring $\lim_{\dot\gamma\to\infty}\eta = \mu_\infty$. Although finite-viscosity models such as Sisko and CHB are suited for high-shear-rate regimes, only the pre-onset region (0.1–200 s^{-1}) was used for model fitting to ensure physical consistency, following the measurement procedure described in Thota Radhakrishnan et al. [71]. Beyond this range, instabilities due to secondary flows are observed in the cup–bob geometry, which are largely unavoidable, being an inherent characteristic of this configuration at high rotational speeds. Future measurements using parallel-plate or vane geometries could help mitigate such effects, thereby extending the valid shear-rate range and enabling a more accurate capture of high-shear-rate asymptotes.

Parameters were estimated by nonlinear least-squares optimization (Levenberg–Marquardt trust-region) applied to logarithmically spaced rheometer data; the free parameters were (m, n) for Sisko and (τ_y, m, n) for CHB. It is worth noting that global optimization methods, such as genetic algorithms (GA), are often employed to avoid local minima and enforce constraints [76,77], but they are computationally expensive. Here, least-squares was sufficient because the rheometric data were dense (≈300 steady points per sweep), reproducible, and smoothly monotonic, yielding a well-behaved residual surface without competing minima. The final fitted parameters are reported in Table 4, and the corresponding flow curves with model fits are shown in Fig. 5, illustrating progressive shear-thinning and the emergence of yield stress at higher concentrations.

2.5. Non-Newtonian Reynolds number

Unlike Newtonian fluids, the viscosity of NNFs is not constant but varies with the shear rate. As a result, applying the traditional definition of the Reynolds number becomes challenging. Apparent-viscosity Reynolds number correlations, such as those proposed by Metzner and Reed [24] and Clapp [78], can provide useful scaling under laminar conditions but fail to represent the underlying physics in turbulent regimes [79]. To overcome this limitation, we employ the wall-viscosity-based Reynolds number, also referred to as the generalized Reynolds number (Re_w), introduced by Rudman et al. [80]. This definition is directly related to the wall shear stress, thereby better characterizing the near-wall region where shear effects are dominant. The generalized Reynolds number is expressed as:

$$Re_w = \frac{\rho U D}{\eta_w} \tag{5}$$

where, ρ is the fluid density, U is the cross-sectional average velocity, and D is the pipe's inner diameter. For CHB, the corresponding wall viscosity (η_w) is

$$\eta_{w,\mathrm{CHB}} = \frac{\tau_y + \mu_\infty\dot\gamma_w + m\dot\gamma_w^{\,n}}{\dot\gamma_w} \tag{6}$$

and, at the wall, $\dot\gamma_w$ is the positive root of

$$\tau_w = \tau_y + \mu_\infty\dot\gamma_w + m\dot\gamma_w^{\,n} \tag{7}$$

Eqs. (6)–(7) recover HB when $\mu_\infty \to 0$ and Sisko when $\tau_y \to 0$. In both cases, $\dot\gamma_w$ is solved numerically using a scalar root-finding algorithm Brent [81]; substituting η_w from Eq. (6) into Eq. (5) gives Re_w. Throughout this article, we employ this definition of the Reynolds number to describe the flow behavior of NNFs.

3. Numerical models

Several numerical approaches have been proposed in recent years with proven accuracy and reliability. However, given the Reynolds-number range considered in this work, high-fidelity methods such as DNS [33,80] and LES [82] were excluded due to their prohibitive computational cost. Likewise, near-wall modeling approaches such as modified damping functions [83], molecular-viscosity closures [84], and fluctuating-viscosity stress tensors [20], were not pursued, as they require much finer grids and substantially higher cost (see Fig. 6). We therefore adopt a wall-function approach as a practical compromise between accuracy and cost.

As outlined in Section 1, we benchmark the experiments against three modeling approaches. For completeness, we begin with the classical Launder–Spalding wall function [57], formulated for Newtonian

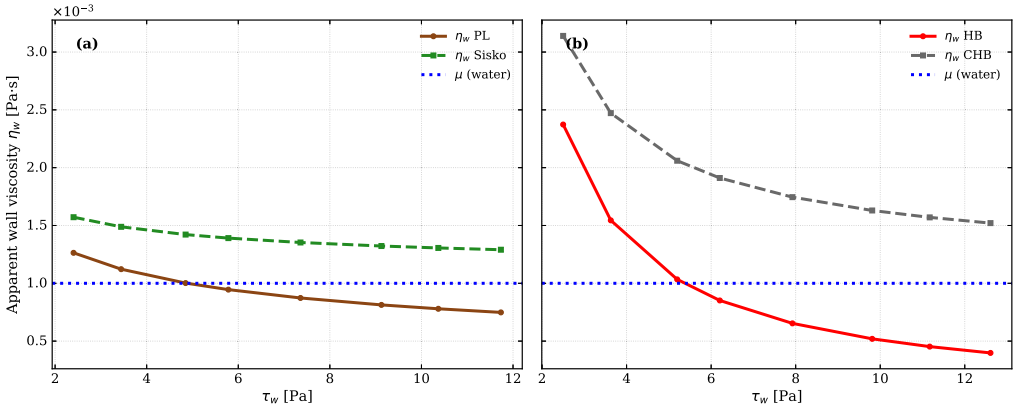

Fig. 4. Apparent wall viscosity η_w as a function of wall shear stress τ_w for two slurry cases. (a) Slurry S3 fitted with Power–Law (PL) and Sisko models; (b) Slurry S5 fitted with Herschel–Bulkley (HB) and Combined Herschel–Bulkley (CHB) models. The horizontal dotted line indicates the viscosity of the carrier fluid (here, water) at the test temperature.

Table 4
Rheological characteristics of the slurry samples fitted with Newtonian, Sisko, and Combined Herschel–Bulkley (CHB) models. For Sisko and CHB, the high–shear viscosity was constrained to the carrier fluid viscosity ($\mu_\infty = 0.001$Pa s).

Slurry	Fitted model	Yield stress (τ_y)	Consistency index (m)	Behavior index (n)
–	–	[Pa]	[Pa s^n]	–
S1	Newtonian	0	0.00144	1.00
S2	Sisko	0	0.00185	0.87
S3	Sisko	0	0.00946	0.62
S4	CHB	0.069	0.0293	0.54
S5	CHB	0.147	0.0961	0.42

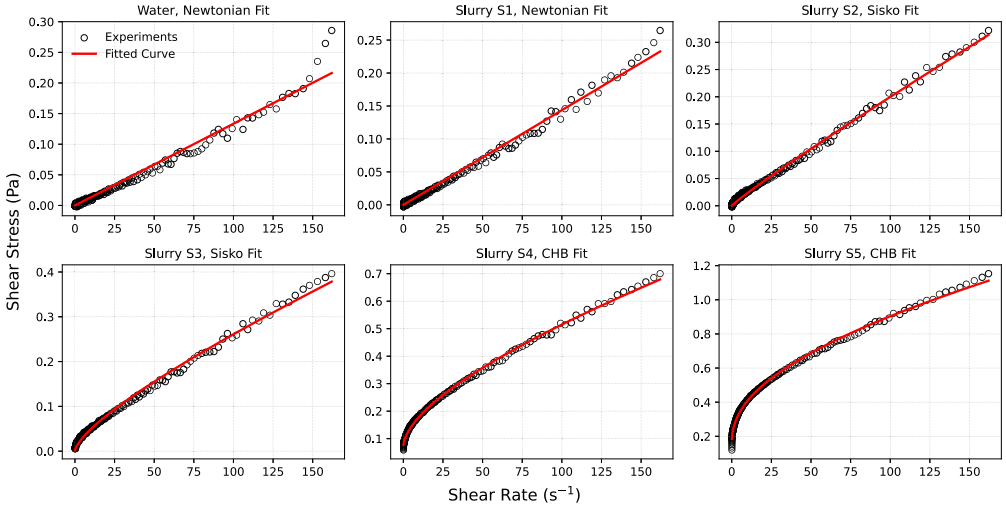

Fig. 5. Shear stress–shear rate Rheograms for water and clay–water slurries (S1–S5). Symbols denote experimental rheometric measurements, while solid lines represent the corresponding fitted models (Newtonian, Sisko, and CHB).

turbulent flows and implemented in the RANS solver to relate mean velocity and wall shear stress. For brevity, we denote this correlation by χ:

$$\frac{u}{(\tau_w/\rho)^{1/2}} = \underbrace{\frac{1}{\kappa}\ln\left\{\frac{y\rho E}{\mu}\left(\frac{\tau_w}{\rho}\right)^{1/2}\right\}}_{\chi} \tag{8}$$

where $\kappa \approx 0.41$ is the von Kármán constant, y is the distance from the wall, μ is the dynamic viscosity, and $E = 9.793$ is an empirical constant. For NNFs, we introduce the generalized (rheology-based) wall function, denoted by ψ:

$$\frac{u}{u_{*,y}} = \underbrace{\frac{1}{\kappa}\ln\left(E\, y^+_{\text{gen}}\right)}_{\psi}, \qquad y^+_{\text{gen}} = \frac{y\,\rho\,u_{*,y}}{\eta_w}, \quad u_{*,y} = \sqrt{\frac{\tau_w - \tau_y}{\rho}} \tag{9}$$

Hence, instead of a constant Newtonian viscosity μ, the velocity scaling in Eq. (9) depends implicitly on the constitutive rheology and on τ_w through $u_{*,y}$ and $\eta_w(\tau_w)$. For the CHB model (Eq. (3)), the parameters (τ_y, m, n) are obtained by fitting the rheometric data, while the wall viscosity η_w is evaluated from Eq. (6) after solving Eq. (7) for $\dot{\gamma}_w$ at

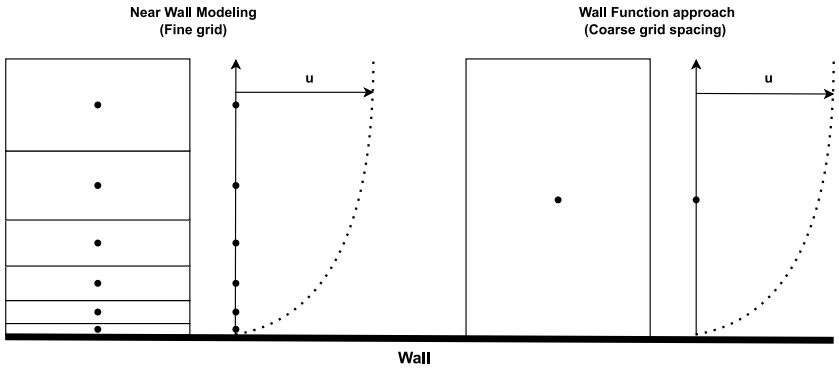

Fig. 6. Near-wall modeling vs. wall function: implementing wall functions significantly reduces computational cost.

the prescribed τ_w. In the limit $\mu_\infty \to 0$, Eq. (9) reduces to Mehta's HB inner scaling [58], given by:

$$\frac{u}{\left(\frac{\tau_w-\tau_y}{\rho}\right)^{1/2}} = \frac{1}{n\kappa}\ln\left[y^n\,\frac{\rho}{m}\,E\left(\frac{\tau_w-\tau_y}{\rho}\right)^{\frac{2-n}{2}}\right] \tag{10}$$

The generalized wall function (ψ) enforces a theoretical constraint at the first cell centroid on the iterated velocity field, ensuring closer agreement with experimental observations. Since ψ is implicit in τ_w, it is implemented as a specified shear boundary condition coupled with the k–ϵ turbulence model. Although a Reynolds stress model could also have been employed, the k–ϵ formulation was selected for its robustness and computational efficiency. Model consistency was verified through a grid-independence study and validation against the analytical laminar HB solution (see Yusufi et al. [13, Fig. 4]), the corresponding plots are omitted here to avoid duplication. All other numerical settings, including the mesh, solver parameters, boundary conditions, and convergence criteria, follow the configuration described in Yusufi et al. [13].

Finally, ψ is compared against the semi-empirical approach of Dodge and Metzner [3], who employed dimensional analysis and similarity with Newtonian correlations [85] to derive a logarithmic velocity profile and a friction factor correlation (hereafter, DM). The DM friction factor is given by

$$f_{\mathrm{DM}} = \left(\frac{4}{(n')^{0.75}}\log_{10}\left(Re_{MR}\,f^{(1-n'/2)}\right) - \frac{0.4}{(n')^{1.2}}\right)^{-2} \tag{11}$$

here, Re_{MR} is the Metzner–Reed Reynolds number [24] given by:

$$Re_{MR} = \frac{\rho\,u^{2-n'}\,D^{n'}}{m'\,8^{(n'-1)}} \tag{12}$$

where n' and m' are obtained using the Rabinowitsch–Mooney procedure [86,87]. The value of n' follows from the slope of the log–log plot of $(\tau-\tau_y)$ versus $\dot{\gamma}$ near the wall shear rate $\dot{\gamma}_w$, while m' is obtained from the corresponding intercept:

$$n' = \left.\frac{d\ln(\tau-\tau_y)}{d\ln\dot{\gamma}}\right|_{\dot{\gamma}=\dot{\gamma}_w} \tag{13}$$

$$m' = \frac{\tau_w-\tau_y}{\dot{\gamma}_w^{\,n'}} = \exp\left(\ln(\tau_w-\tau_y) - n'\,\ln\dot{\gamma}_w\right) \tag{14}$$

The corresponding inner scaling and velocity profile use n' and m' likewise:

$$u^+ = \frac{5.66}{(n')^{0.75}}\ln y^+ - \frac{0.4}{(n')^{1.2}} + \frac{2.458}{(n')^{0.75}}\left[1.960+1.255\,n'-1.628\,n'\,\ln\left(3+\frac{1}{n'}\right)\right] \tag{15}$$

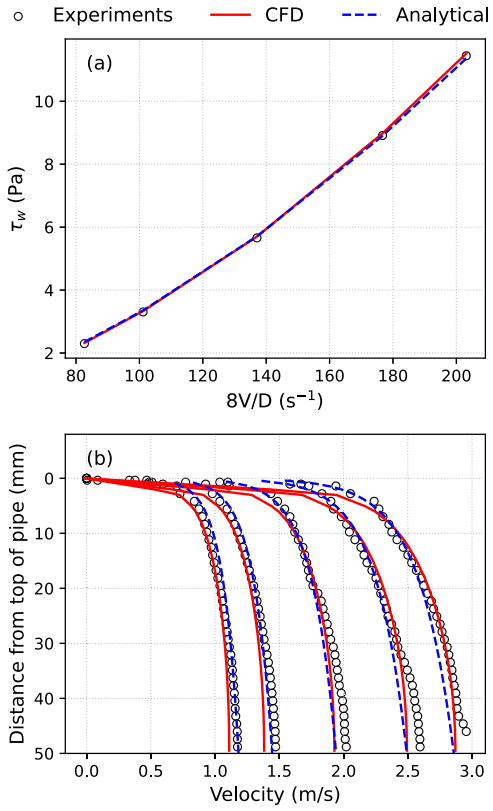

Fig. 7. Verification of experimental setup. (a) Comparison of wall shear stress measurements with CFD (ψ/χ) and the Darcy–Weisbach equation for water. (b) Time-averaged velocity profiles obtained from UVP, compared with CFD (ψ/χ) and the logarithmic law of the wall for Slurry S1 (Newtonian fluid).

Here, the non-dimensional velocity (u^+) and wall distance (y^+) are defined as

$$u^+ = \frac{u}{u_\tau}, \qquad y^+ = \frac{y\,u_\tau}{\eta_w} \tag{16}$$

where u is the mean axial velocity, y is the distance from the pipe wall, $u_\tau = \sqrt{\tau_w/\rho}$ is the friction velocity, and η_w is the wall viscosity as defined in Eq. (6).

4. Results and discussion

4.1. Wall shear stress

We begin by checking the consistency of the experimental setup by comparing the measured wall shear stress for water with both the

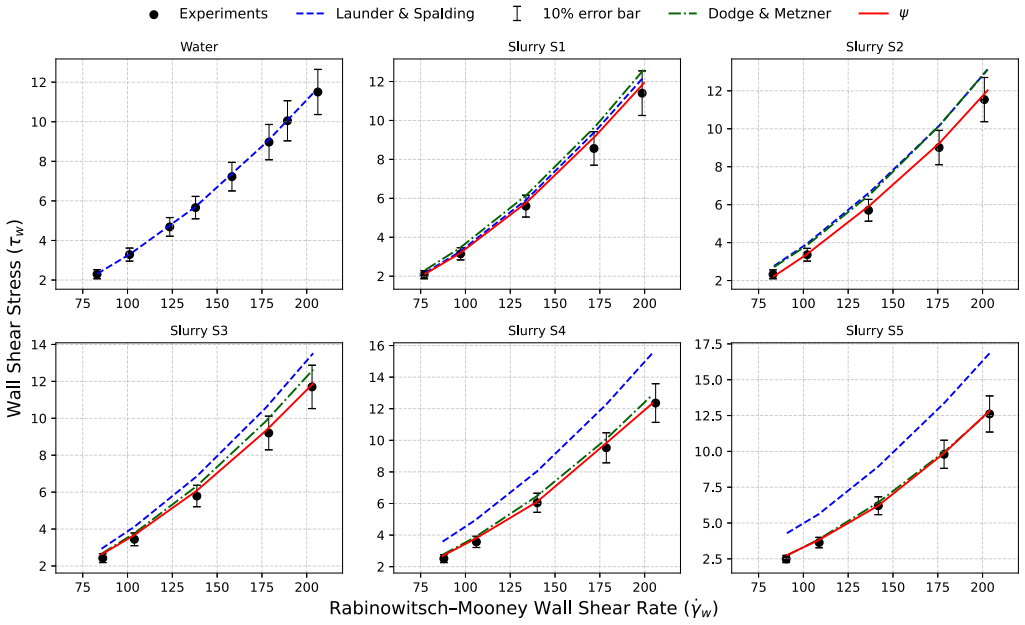

Fig. 8. Wall shear stress (τ_w) as a function of the Rabinowitsch–Mooney wall shear rate ($\dot{\gamma}_w$, Eq. (17)) for water and clay–water slurries at various concentrations.

Darcy–Weisbach prediction and the CFD results (Fig. 7a). It should be noted that, for a Newtonian fluid ($n = 1$, $m = \mu$, $\tau_y = 0$), the generalized wall function ψ reduces exactly to the classical correlation χ. The measured wall shear stress was found to be within the accuracy range of the pressure transducers, which is ±2%.

Fig. 8 illustrates the wall shear stress as a function of the Rabinowitsch–Mooney wall shear rate ($\dot{\gamma}_w$) for water and clay–water slurries (S1–S5), where the nominal value $8V/D$ was corrected for non-Newtonian fluids using the Rabinowitsch–Mooney relation [88], given by:

$$\dot{\gamma}_w = \frac{3n'+1}{4n'}\left(\frac{8V}{D}\right) \tag{17}$$

The measured data are compared with the predicted wall shear stress from Dodge and Metzner [3], the Newtonian-based Launder and Spalding wall function χ (Eq. (8)), and the rheology-based wall function ψ (Eq. (9)). A 10% comparison band is shown to visualize deviations between models and experiments.

We observe that ψ significantly improves the accuracy of wall shear stress predictions, with most data points deviating by no more than 10% from experimental values. Quantitatively, the mean absolute error (MAE), Root mean square error (RMSE), and R^2 values against the experimental data are 0.0634, 0.1194, and 0.9639, respectively. The improvement is most evident at high shear stress levels across all concentrations and in nearly all high shear rate cases. The function enforces a theoretical constraint on the simulated near-wall velocity field, where viscous stresses dominate and velocity gradients are steepest, thereby guiding the solver toward solutions that remain physically consistent with experiments.

This stems from Clapp [78], who demonstrated that a majority of the mean velocity contribution originates near the wall, specifically where the relative radial distance $r/R > 0.8$. In contrast, the central region of the pipe ($r/R \leq 0.8$) contributes only around 7% to the overall velocity. A key distinction from earlier implementations [13,58] is the use of CHB and Sisko models instead of HB and PL, respectively, which ensure that the apparent viscosity remains bounded from below by the viscosity of the continuous phase (water in this case), thereby preventing unphysical values at high shear rates.

In order to understand the Launder and Spalding [57] wall function, χ, and its monotonic increase in predicted wall shear stress with stronger shear-thinning and yield effects (as observed when transitioning from slurry S1 to S5), it is important to recall the near-wall mechanics of non-Newtonian fluids. Very close to the wall, shear rates are high; for shear-thinning rheologies, this leads to lower apparent viscosities and, consequently, enhanced viscous stresses and steeper velocity gradients [89]. In real non-Newtonian turbulence, part of this stress is carried by the viscous contribution, while the Reynolds stresses are reduced relative to Newtonian turbulence [90]. However, the Newtonian-based correlation χ, which assumes a constant viscosity and zero yield stress, cannot capture this redistribution. To compensate for the steeper gradients while maintaining the log-law formulation, the model artificially increases the wall shear stress by inflating the friction velocity. As a result, χ produces a positive bias that grows systematically with increasing slurry concentration.

Lastly, the performance of the Dodge and Metzner [3] correlation (DM) is more subtle. At lower concentrations (S1–S3), DM systematically overpredicts the wall shear stress, with deviations increasing at higher flow rates. Although DM was originally calibrated for power-law rheologies, its formulation with Rabinowitsch–Mooney corrections allows application to purely viscous shear-thinning fluids. In our case, however, the use of Sisko and CHB rheologies caps the apparent viscosity at a minimum equal to that of the carrier fluid. This raises the effective viscosity compared to a pure PL extrapolation (see Fig. 4), lowering the Re_{MR} and driving DM toward overprediction. Surprisingly, at higher concentrations (slurries S4–S5), DM predictions fall within the ±10% tolerance range, in some cases closely matching the experiments.

This behavior indicates a nuanced performance of DM: the correlation provides reasonable agreement even in regimes where its theoretical validity is limited (HB-like slurries), yet tends to overpredict for lower concentrations closer to its nominal range (PL-like slurries). Overall, while DM can offer acceptable estimates under certain conditions, its predictive consistency across different rheological regimes in turbulent non-Newtonian flows appears limited. Table 5 summarizes the error metrics and enables a direct quantitative comparison of the three approaches for both wall shear stress and velocity profiles.

In summary, while ψ provides superior estimates overall, some discrepancies are observed at low shear rates. These deviations likely stem from the fact that ψ still relies on Newtonian-based model constants (κ&E), which need to be calibrated for NNFs. However, tuning these constants requires additional experimental and numerical studies,

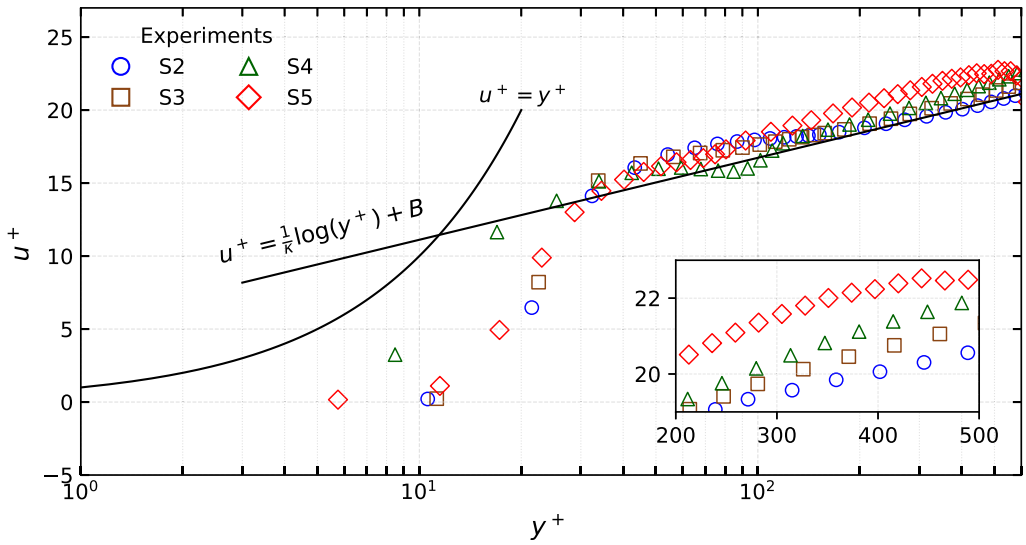

Fig. 9. Mean velocity profiles (in wall units) at flow rate Q1 for slurries S2–S5, highlighting deviations from Newtonian behavior. UVP measurements are shown as scatter points, with solid lines indicating the Newtonian sublayer and log-law reference curves, and a dotted vertical line marking their intersection at $y^+ \approx 11.6$. The inset zooms into the near-wall region to compare the behavior of different slurry concentrations.

which are currently limited. Further, we utilize the $k-\epsilon$ turbulence model to conduct more robust and cost-efficient simulations, rather than the more advanced Reynolds Stress Model. Given the high turbulence intensities in our study, the Reynolds Stress Model, due to its anisotropic treatment of turbulence, would be a more suitable choice for capturing shear stress variations in NNFs [91]. This has been demonstrated in [58], where it was shown that using the Reynolds Stress Model improved the accuracy of wall shear stress predictions.

4.2. Velocity profiles

Velocity profiles were measured at five different flow rates (Q1–Q5, see Table 1), corresponding to average flow velocities ranging from 1.04 m/s to 2.53 m/s. The instantaneous velocity profiles were averaged over a conservative 5-minute interval, chosen to ensure statistically consistent mean values across all slurry concentrations. The vertical position along the pipe's cross-sectional diameter was derived by taking the cosine component of the distance from the transducer axis, as shown in Fig. 2. To verify the accuracy of the ultrasonic velocity profiling (UVP), the flow rate was independently computed by integrating the time-averaged velocity profiles across the pipe diameter and compared with flow meter readings. The close agreement between these methods confirms the reliability of the UVP measurements.

Fig. 7b presents the experimentally measured axial velocity profiles (UVP) for slurry S1, alongside numerical simulations and analytical predictions, plotted as a function of distance from the pipe wall. Since S1 behaves as a Newtonian fluid, it is expected to follow the logarithmic law of the wall. The experimental velocity profiles align closely with both simulations and analytical results, with minimal deviations. Small discrepancies near the pipe center at higher velocities are likely due to attenuation of the ultrasound pulse.

Following this, Fig. 9 illustrates the mean velocity profiles in wall units (u^+ versus y^+, as defined in Eq. (16)) at flow rate Q1 for Slurries S2–S4. For reference, the Newtonian law of the wall is also shown: $u^+ = y^+$ in the viscous sublayer and $u^+ = (1/\kappa)\ln(y^+) + B$ ($\kappa = 0.41$, $B \approx 5.6$) in the log-law region. This provides a baseline for identifying deviations introduced by shear-thinning and yield-stress behavior and highlights their influence on turbulence structure. The discussion here focuses on the log-law region, as experimental limitations prevented the resolution of the viscous sublayer, which is addressed later in this section.

The experimental observations reveal two distinct trends in the behavior of shear-thinning fluids under turbulent flow. Firstly, we observe that the transition to the log-law region is delayed, which means that the intersection of linear and logarithmic profiles is further shifted from $y^+ \approx 11.6$. This aligns with the hypothesis of Wilson and Thomas [5], which attributes the thickening of the sublayer to an increase in the size of dissipative micro-eddies, leading to an expansion of the laminar sublayer. Secondly, while the slope of the log-law region remains approximately $1/\kappa$, we observe an upward shift in the log-law intercept, which increases monotonically with slurry concentration, thus reflecting stronger shear-thinning and yield-stress effects.

This trend is consistent with DNS simulations by Singh et al. [90], who showed that as one moves away from the wall, the shear rate decreases, leading to higher apparent viscosities and correspondingly larger mean viscous stresses than in Newtonian fluids. Because viscosity is not constant but shear-rate dependent, an additional fluctuating-viscosity stress term arises, which acts negatively and reduces the effective Reynolds stresses. Since the total shear stress must remain constant, this stress redistribution results in steeper mean velocity gradients. The outcome is a systematic upward shift of the log-law with increasing non-Newtonian character [92].

Fig. 10 presents the experimental velocity profiles (scatter) alongside model predictions from χ (dashed) and ψ (solid), with each subplot corresponding to one of the four non-Newtonian slurries (S2–S5). For each slurry, five flow rates ($Q1$–$Q5$) are shown. To prevent overlap, the profiles are vertically offset by fixed increments of 10 units: $Q1$ is plotted without offset, whereas $Q2$–$Q5$ are successively shifted by +10, +20, +30, and +40 units, respectively. The left axis therefore represents the shifted u^+ values, while the right axis marks the zero-reference level, $0(Q_i)$, for each flow rate.

For χ, a systematic underprediction relative to the experiments is observed. This discrepancy is small for the weakly non-Newtonian slurry S2 but becomes increasingly pronounced as shear-thinning and yield-stress effects intensify. The bias originates from an overestimation of the wall shear stress (see Fig. 8), which lowers the predicted u^+ values for a given y^+. As discussed in the previous subsection, these discrepancies stem from the assumption of constant viscosity, which fails to account for the upward shift induced by shear-thinning effects. In contrast, ψ exhibits good agreement with the experimental profiles for $y^+ > 100$. Closer to the wall, however, ψ tends to underpredict the velocities, with deviations particularly evident for $y^+ < 60$. These near-wall discrepancies diminish progressively as slurry concentration

Table 5
Model-experiment performance summary for wall shear stress and velocity profiles.

	Wall shear stress τ_w			Velocity profiles (U vs. y)		
Approach	MAE [Pa]	RMSE [Pa]	R^2	MAE [m/s]	RMSE [m/s]	R^2
ψ [58]	0.2005	0.2353	0.9952	0.0634	0.1194	0.9639
χ [57]	1.4825	1.5991	0.7527	0.0751	0.1367	0.9526
DM [3]	0.5455	0.6010	0.9651	0.1479	0.2048	0.8937

Note. Experimental uncertainties, such as for UVP, follow a GUM analysis as in [52]; pressure-transducer accuracy is ±2% (applied to each τ_w point); the flow meter is ±5%; the temperature probe is ±0.04%, as discussed in the methodology section.

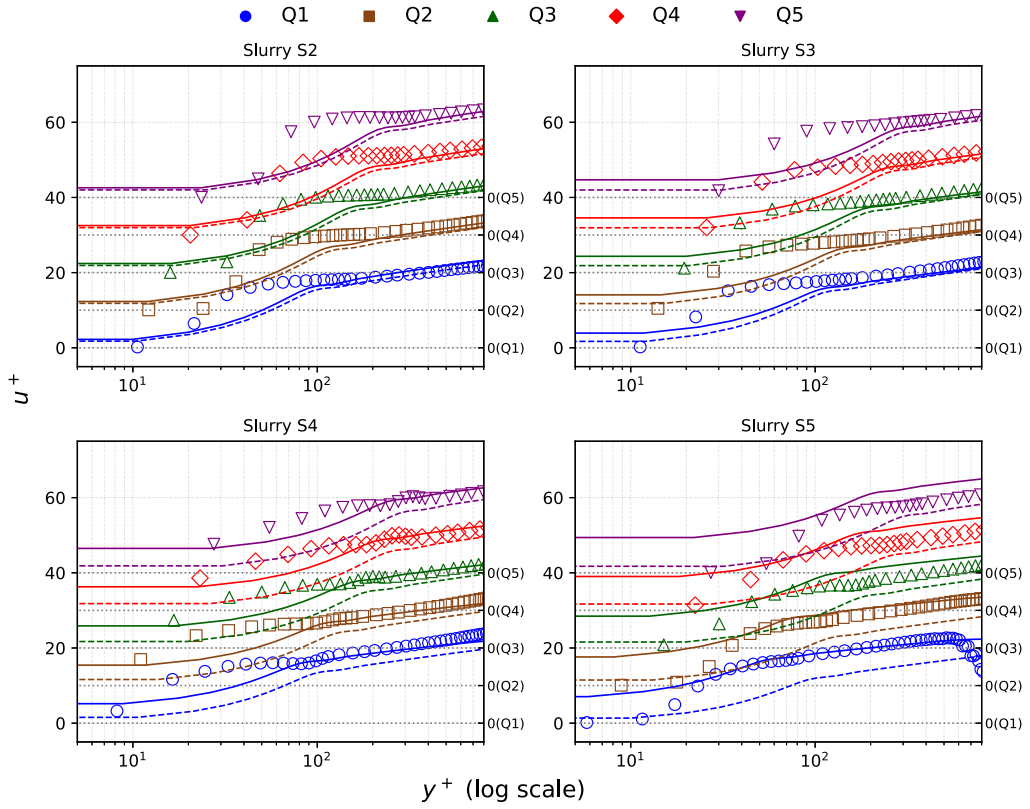

Fig. 10. Comparison of mean velocity profiles in wall units for slurries S2–S5. Experimental data are shown as scatter points, while solid and dotted lines denote predictions with ψ and χ, respectively. Profiles for different flow rates ($Q1$–$Q5$) are vertically offset by increments of 10 for clarity, with the corresponding baselines indicated on the right axis. The legend shows the marker shape and color associated with each flow rate.

increases, and for the highest concentration case (S5), ψ reproduces the experimental data well down to $y^+ \approx 30$.

The reasons for these discrepancies are two-fold. First, in our numerical models, the y^+ values are confined to the log-law region, typically set between 60 and 200. Below $y^+ < 60$, the velocity profile between the first cell centroid and the wall is approximated using the wall viscosity (see Eq. (6)). However, this may not accurately depict the true velocity gradient between the wall and the first cell centroid. A possible solution is to employ more wall-resolved models, such as $k-\omega$ as in [21] or modified damping functions as in [18,83], or utilize DNS [33,80]. However, this requires much finer grids, consequently increasing the computational cost and hence restricting going beyond certain levels of turbulence (see [23] for detailed discussion).

Second, our experiments employ a non-invasive approach to capture velocity profiles using a 4 MHz frequency transducer, while this could be improved by utilizing higher-frequency transducers (e.g., 8 MHz) or optimizing velocity estimation algorithms (see [55]). However, the first involves a trade-off between spatial resolution and penetration depth, while the second increases complexity. Additionally, various intrinsic factors (such as pulse repetition frequency, fundamental frequency, pulse time-lapse, and fluid sound speed) and extrinsic factors (including transducer positioning, inclination angle, echoes from the pipe wall, the use of ultrasound gel, and positional shifts due to vibrations and gel viscosity) also contribute to these discrepancies, as highlighted in [52]. Nonetheless, for $y^+ > 60$, the rheology-based wall function significantly enhances the prediction of velocity profiles compared to Newtonian-based solvers.

Finally, Fig. 11 presents the velocity profiles from a global perspective, where the x-axis shows the time-averaged velocity (m/s) and the y-axis the vertical distance from the transducer (mm). Here, $y = 0$ corresponds to the inner pipe wall at the transducer location. With increasing slurry concentration, the measurable penetration depth decreased, and the signal became noisier. Under comparable experimental conditions, Dash and Poelma [2] reported a critical settling velocity of approximately 1 m/s for clay–water slurries. Since the velocity range in our study lies well above this threshold, particle settling is not expected, and the velocity distribution can reasonably be assumed to remain symmetrical. Accordingly, only the upper half of the pipe was considered for this study.

The experimental results are compared with numerical simulations using the wall function, ψ (solid lines), and with Dodge and Metzner [3] model (dashed lines). Consistent with the trends observed in wall shear stress, the ψ estimates the velocity profiles reasonably well. However, some discrepancies are evident, particularly near the pipe

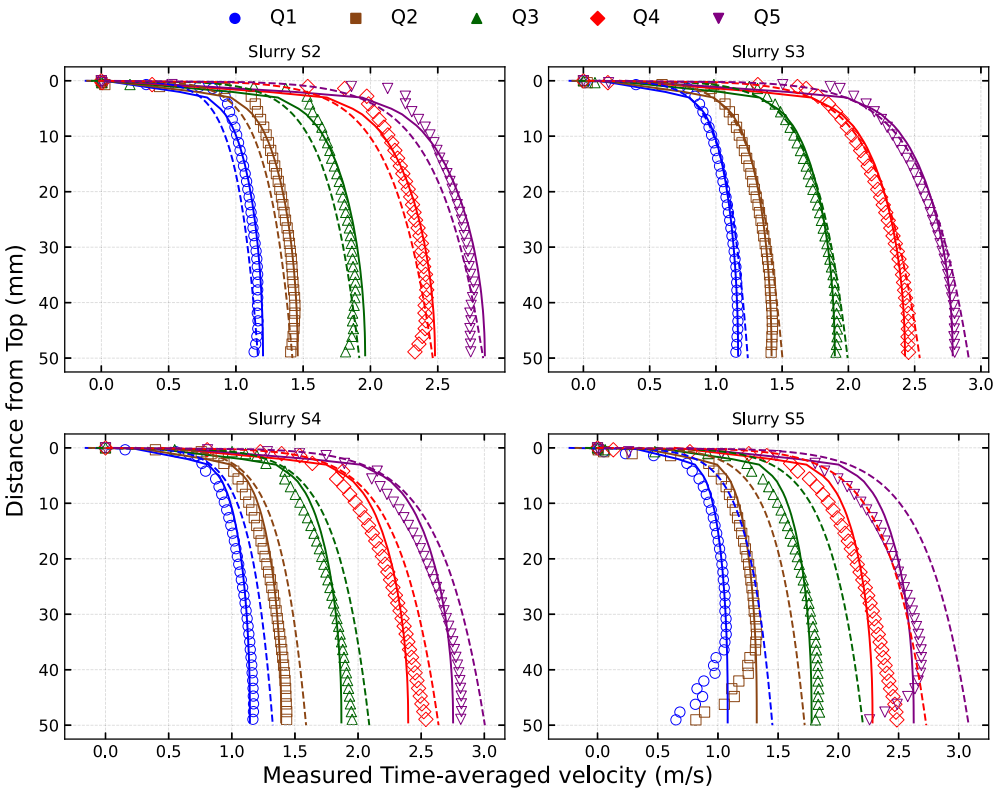

Fig. 11. Comparison of time-averaged velocity profiles measured using UVP with model predictions for slurries S2–S5. Scatter points indicate experimental data, while solid and dotted lines represent predictions from ψ and Dodge and Metzner [3], respectively. The legend shows the scatter shapes and colors corresponding to each flow rate.

center. As the concentration increases (Slurries S4 and S5), particularly at higher flow rates (Q4 and Q5 for S4 and Q3, Q4, and Q5 for S5), the ψ deviates more significantly from the experimental results. These discrepancies mainly arise from attenuation at high velocities, which limits ultrasound penetration depth [2]. Additionally, higher particle concentrations introduce heterogeneities due to particle collisions, shear-induced particle migration, density differentials, and floc formation resulting from frictional interactions among particles [93].

In contrast, DM performs reasonably well at low concentrations (slurry S2), with its best agreement observed for slurry S3. However, as the concentration increases (S4–S5), the near-wall velocity gradients predicted by DM become noticeably steeper than those measured experimentally. This behavior is somewhat unexpected: although the DM correlation yields wall-shear-stress values close to the experimental data at higher concentrations (Fig. 8), the corresponding bulk velocity profiles deviate more substantially. In principle, accurate wall-shear-stress predictions should be accompanied by similar trends in near-wall velocity gradients, yet this consistency is not observed. Consequently, the velocity profiles diverge progressively with increasing concentration, despite the apparent agreement in τ_w. These observations suggest that DM may reproduce wall-shear-stress magnitudes without fully capturing the associated velocity distribution, indicating constraints associated with the limited experimental dataset.

Finally, we assess the applicability of the three modeling approaches against the experimental data, with their quantitative performance summarized in Table 5. The experimental uncertainties, arising from pressure transducers and flow instrumentation, were discussed earlier in the methodology section, while those associated with UVP measurements can be evaluated following a GUM analysis [52]. Overall, ψ shows the best overall consistency with the experimental results, exhibiting the lowest errors for both wall shear stress and velocity profiles, with R^2 values exceeding 0.96 in both cases. χ tends to underperform for τ_w, reflecting its structural limitation in capturing shear-thinning and yield effects, although its velocity predictions remain reasonably correlated with the experiments. The DM correlation exhibits intermediate behavior, reproducing τ_w more accurately than χ but displaying larger deviations in the velocity profiles, consistent with the earlier discussion. Taken together, these observations indicate that ψ offers a consistent and scalable framework for predicting both wall shear stress and velocity profiles, with potential applicability to industrial non-Newtonian flow systems.

5. Conclusion and outlook

This study investigated the wall shear stress and velocity profiles of non-Newtonian clay–water slurries under turbulent flow conditions. By combining non-invasive Ultrasonic Velocity Profiling (UVP) measurements in an industrial-scale pipe loop with CFD simulations and model comparisons, new insights were obtained into the hydrodynamics of shear-thinning and viscoplastic slurries. The experiments revealed a systematic upward shift in the log-law region with increasing concentration, accompanied by a delayed transition to turbulence, indicating a redistribution of shear stresses as non-Newtonian effects become more pronounced.

Benchmarking against the three models showed that the rheology-based wall function (ψ) provided the most consistent agreement with experimental data, with small deviations and R^2 values exceeding 0.96 for both wall shear stress and velocity profiles. The Dodge–Metzner correlation (DM) demonstrated intermediate performance, offering reasonable estimates of wall shear stress but showing less consistency in reproducing velocity distributions. The classical Launder–Spalding wall function (χ) tended to underpredict τ_w due to its constant-viscosity assumption, although its velocity profiles remained moderately correlated with the experiments.

In the near-wall sublayer and buffer regions ($y^+ < 60$), ψ approximates the velocity profile using a non-Newtonian wall viscosity, assuming the first computational cell lies within the log-law region. Although

this approach improves overall predictions, it may not fully capture the near-wall profile, suggesting the need for a more detailed wall model. These discrepancies arise from both the limitations of numerical models to capture near-wall gradients at high Reynolds numbers and experimental constraints, such as ultrasound attenuation and particle heterogeneities at higher concentrations. Further advancements, such as combining high-resolution near-wall measurements, such as echo-PIV [2,40], with high-fidelity numerical studies, are needed to better understand the physics and fine-tune the model constants, thereby improving accuracy for turbulent non-Newtonian models.

A key implication of these findings is that turbulence closures for non-Newtonian flows can only perform well if supported by precise rheological characterization. For the highly turbulent flows considered here, rheological measurements should ideally extend to at least twice the maximum shear rate expected in the pipe, as recommended by Singh et al. [94]. Although we mitigated this limitation by adopting infinite-viscosity extensions (e.g., CHB/Sisko), future work should incorporate high-shear-rate rheometry to strengthen model calibration and predictive accuracy. Overall, this study reinforces the importance of integrating accurate rheological characterization with turbulence modeling to enable reliable and scalable predictions of non-Newtonian slurry transport in industrial pipelines.

Finally, it is important to acknowledge the limitations of this study. While this work employed the non-invasive Doppler-based UVP method to generate velocity profiles, the device has limitations in capturing steep velocity gradients near the wall. These become more evident as flow velocity and particle concentration increase, as reflected in the near-wall plots presented herein. This issue could potentially be mitigated by using higher-frequency transducers or optimized velocity estimation algorithms [55]; however, the former involves a trade-off with penetration depth, while the latter increases system complexity.

Additionally, the device is sensitive to transducer position and Doppler angle. Other factors, such as multiple echoes from the wall or floc formation due to particle friction, may also contribute to measurement errors. As shown by Furuichi [52], these effects can introduce uncertainties of up to 2.16%. Further, while the present work examined concentrated kaolin slurries (up to 19% by weight), their yield stresses remained small relative to the wall shear stress, limiting their suitability as high-yield analogues. A potential alternative is to use well-characterized Herschel–Bulkley fluids such as Carbopol, although this would substantially increase costs given the scale of the experimental setup.

Lastly, this study was conducted in a 100-mm diameter pipe loop. In practical applications, pipe diameters vary significantly across different sections of pipelines, which can influence the distribution of shear stress and flow behavior. Future studies should investigate the impact of diameter variations on slurry transport to improve the broader applicability of these findings across industrial systems.

CRediT authorship contribution statement

B.K. Yusufi: Writing – review & editing, Writing – original draft, Visualization, Validation, Methodology, Investigation, Data curation, Conceptualization. **Z. Kapelan:** Writing – review & editing, Supervision, Resources, Project administration. **D. Mehta:** Writing – review & editing, Supervision, Resources, Project administration, Investigation, Funding acquisition, Conceptualization.

Funding

This research was supported by the Department of Water Management at Delft University of Technology, Netherlands.

Ethics approval and consent to participate

Not applicable.

Consent for publication

Not applicable.

Materials availability

Not applicable.

Declaration of competing interest

The authors declare that they have no known competing financial interests or personal relationships that could have appeared to influence the work reported in this paper.

Acknowledgments

We sincerely thank Deltares (Hydraulics for Industry and Infrastructure), Delft, The Netherlands, for hosting and supporting the measurement campaign, the Hydro-Hall team, particularly Michiel Tukker, for permitting us to use the experimental facility, and Gosse Oldenziel for his assistance during the measurements and insightful discussions. All authors contributed to manuscript revisions and approved the final version.

Data availability

Data will be made available on request.

References

[1] Mehmet Sorgun, Tevfik Denizhan Muftuoglu, Ismail Hakki Gucuyener, Friction factor estimation for turbulent flow of Herschel-Bulkley and power law fluids in pipes, J. Pet. Sci. Eng. (ISSN: 0920-4105) 211 (2022) 110044, http://dx.doi.org/10.1016/J.PETROL.2021.110044.

[2] Amitosh Dash, Christian Poelma, Long-time-scale transients in an industrial-scale slurry pipeline near the laminar-turbulent transition, Flow 2 (2022) http://dx.doi.org/10.1017/flo.2022.18, E25.

[3] D.W. Dodge, A.B. Metzner, Turbulent flow of non-newtonian systems, AIChE J. (ISSN: 15475905) 5 (2) (1959) http://dx.doi.org/10.1002/aic.690050214.

[4] B.M. Torrance, Friction factors for turbulent non-Newtonian fluid flow in circular pipes, South Afr. Mech. Eng. 13 (1963) 89–91.

[5] Kenneth C. Wilson, Allan D. Thomas, A new analysis of the turbulent flow of non-newtonian fluids, Can. J. Chem. Eng. (ISSN: 1939019X) 63 (4) (1985) http://dx.doi.org/10.1002/cjce.5450630403.

[6] P.T. Slatter, Modelling the turbulent flow of non-Newtonian slurries, R-and-D J. (ISSN: 03019322) 12 (2) (1996) http://dx.doi.org/10.1016/s0301-9322(97)80150-4.

[7] PS Gnambode, P Orlandi, Meryem Ould-Rouiss, Xavier Nicolas, Large-eddy simulation of turbulent pipe flow of power-law fluids, Int. J. Heat Fluid Flow 54 (2015) 196–210, http://dx.doi.org/10.1016/j.ijheatfluidflow.2015.05.004.

[8] Noman Yousuf, Nimmi Kurukulasuriya, Andrew Chryss, Murray Rudman, Catherine Rees, Shane Usher, Ehsan Farno, Daniel Lester, Nicky Eshtiaghi, An accurate and robust method for intensification of wastewater sludge pipe flow, Sci. Total Environ. 949 (2024) 175143, http://dx.doi.org/10.1016/j.scitotenv.2024.175143.

[9] Yamid J García-Blanco, Vitor Y Urazaki, Angel DJ Rivera, Luis H Quitian, Eduardo M Germer, Admilson T Franco, Rheological characterization of viscoplastic fluid flow in a pipe with wall slip using in situ particle image velocimetry, Rheol. Acta 62 (2) (2023) 93–110.

[10] Dilhan Kalyon, Apparent slip and viscoplasticity of concentrated suspensions, J. Rheol. - J RHEOL 49 (2005) 621–640, http://dx.doi.org/10.1122/1.1879043.

[11] K.M. Assefa, D.R. Kaushal, A comparative study of friction factor correlations for high concentrate slurry flow in smooth pipes, J. Hydrol. Hydromechanics (ISSN: 13384333) 63 (1) (2014) http://dx.doi.org/10.1515/johh-2015-0008.

[12] Dhruv Mehta, Adithya Krishnan Thota Radhakrishnan, Jules B. van Lier, Francois H.L.R. Clemens, Assessment of numerical methods for estimating the wall shear stress in turbulent Herschel–Bulkley slurries in circular pipes, J. Hydraul. Res. (ISSN: 00221686) 59 (2) (2021) http://dx.doi.org/10.1080/00221686.2020.1744751.

[13] B.K. Yusufi, Z. Kapelan, D. Mehta, Rheology-based wall function approach for wall-bounded turbulent flows of Herschel–Bulkley fluids, Phys. Fluids (ISSN: 1070-6631) 36 (2) (2024) 023112, http://dx.doi.org/10.1063/5.0180663, URL arXiv:https://pubs.aip.org/aip/pof/article-pdf/doi/10.1063/5.0180663/19684079/023112_1_5.0180663.pdf.

[14] N. El-Emam, A.H. Kamel, M. El-Shafei, A. El-Batrawy, New equation calculates friction factor for turbulent flow on non-Newtonian fluids, Oil & Gas J. 101 (36) (2003) 74.

[15] Sercan Gul, Mitchell David Johnson, Ali Karimi Vajargah, Zheren Ma, Besmir Buranaj Hoxha, Eric van Oort, A data driven approach to predict frictional pressure losses in polymer-based fluids, in: SPE/IADC Drilling Conference, Proceedings, 2019-March, 2019, http://dx.doi.org/10.2118/194132-ms.

[16] Nigel Heywood, D. Cheng, Comparison of methods for predicting head loss in turbulent pipe flow of non-Newtonian fluids, Trans. Inst. Meas. Control 6 (1984) 33–45, http://dx.doi.org/10.1177/014233128400600105.

[17] M.R. Malin, Turbulent pipe flow of power-law fluids, Int. Commun. Heat Mass Transfer (ISSN: 07351933) 24 (7) (1997) http://dx.doi.org/10.1016/S0735-1933(97)00083-3.

[18] Artur Bartosik, Application of rheological models in prediction of turbulent slurry flow, Flow, Turbul. Combust. (ISSN: 13866184) 84 (2) (2010) http://dx.doi.org/10.1007/s10494-009-9234-y.

[19] F.T. Pinho, A GNF framework for turbulent flow models of drag reducing fluids and proposal for a k-ϵ type closure, J. Non-Newton. Fluid Mech. (ISSN: 03770257) 114 (2–3) (2003) http://dx.doi.org/10.1016/S0377-0257(03)00120-4.

[20] Andrey A. Gavrilov, Valeriy Ya Rudyak, Reynolds-averaged modeling of turbulent flows of power-law fluids, J. Non-Newton. Fluid Mech. (ISSN: 03770257) 227 (2016) http://dx.doi.org/10.1016/j.jnnfm.2015.11.006.

[21] S. Lovato, G.H. Keetels, S.L. Toxopeus, J.W. Settels, An eddy-viscosity model for turbulent flows of Herschel–Bulkley fluids, J. Non-Newton. Fluid Mech. (ISSN: 03770257) 301 (2022) http://dx.doi.org/10.1016/j.jnnfm.2021.104729.

[22] E. Amani, A. Ahmadpour, M.J. Aghajari, Large-eddy simulation of turbulent non-Newtonian flows: A comparison with state-of-the-art RANS closures, Int. J. Heat Fluid Flow 99 (2023) 109076.

[23] B.K. Yusufi, Z. Kapelan, D. Mehta, Advances in modeling the flow of Herschel–Bulkley fluids in pipes: A review, Phys. Fluids (ISSN: 1070-6631) 37 (2) (2025) 021302, http://dx.doi.org/10.1063/5.0252248, URL http://dx.doi.org/10.1063/5.0252248.

[24] A.B. Metzner, J.C. Reed, Flow of non-newtonian fluids—correlation of the laminar, transition, and turbulent-flow regions, AIChE J. (ISSN: 15475905) 1 (4) (1955) http://dx.doi.org/10.1002/aic.690010409.

[25] Christian Poelma, Measurement in opaque flows: a review of measurement techniques for dispersed multiphase flows, Acta Mech. 231 (6) (2020) 2089–2111, http://dx.doi.org/10.1007/s00707-020-02683-x.

[26] B. Güzel, T. Burghelea, I.A. Frigaard, D.M. Martinez, Observation of laminar-turbulent transition of a yield stress fluid in Hagen-Poiseuille flow, J. Fluid Mech. (ISSN: 14697645) 627 (2009) http://dx.doi.org/10.1017/S0022112009005813.

[27] Antoine Charles, Jorge Peixinho, Thierry Ribeiro, Sam Azimi, Vincent Rocher, Jean-Christophe Baudez, S Amir Bahrani, Asymmetry and intermittency in the rheo-inertial transition to turbulence in pipe flow, Phys. Fluids 36 (5) (2024) http://dx.doi.org/10.1063/5.0211807.

[28] J.T. Park, R.J. Mannheimer, T.A. Grimley, T.B. Morrow, Pipe flow measurements of a transparent non-newtonian slurry, J. Fluids Eng. Trans. the ASME (ISSN: 1528901X) 111 (3) (1989) http://dx.doi.org/10.1115/1.3243648.

[29] M.P. Escudier, F. Presti, Pipe flow of a thixotropic liquid, J. Non-Newton. Fluid Mech. (ISSN: 03770257) 62 (2–3) (1996) http://dx.doi.org/10.1016/0377-0257(96)01417-6.

[30] Jorge Peixinho, C. Nouar, C. Desaubry, B. Théron, Laminar transitional and turbulent flow of yield stress fluid in a pipe, J. Non-Newton. Fluid Mech. (ISSN: 03770257) 128 (2–3) (2005) http://dx.doi.org/10.1016/j.jnnfm.2005.03.008.

[31] H. Blasius, Das Aehnlichkeitsgesetz bei Reibungsvorgängen in Flüssigkeiten, in: Mitteilungen Über Forschungsarbeiten Auf Dem Gebiete Des Ingenieurwesens, Springer Berlin Heidelberg, Berlin, Heidelberg, 1913, pp. 1–41, http://dx.doi.org/10.1007/978-3-662-02239-9{_}1.

[32] C.F. Colebrook, Turbulent flow in pipes, with particular reference to the transition region between the smooth and rough pipe laws, J. Inst. Civ. Eng. 11 (4) (1939) http://dx.doi.org/10.1680/ijoti.1939.13150.

[33] Jagmohan Singh, Turbulent flow of Generalised Newtonian fluids through pipes and open channels (Ph.D. thesis), Monash University, Australia, 2017, http://dx.doi.org/10.4225/03/59704ea0143da, URL https://bridges.monash.edu/articles/thesis/Turbulent_flow_of_Generalised_Newtonian_fluids_through_pipes_and_open_channels/5220175.

[34] Rodrigo S Mitishita, Jordan A MacKenzie, Gwynn J Elfring, Ian A Frigaard, Fully turbulent flows of viscoplastic fluids in a rectangular duct, J. Non-Newton. Fluid Mech. (ISSN: 0377-0257) 293 (2021) 104570, http://dx.doi.org/10.1016/j.jnnfm.2021.104570.

[35] Yamid J García-Blanco, E Mancilla, Eduardo M Germer, Admilson T Franco, A PIV investigation of laminar and turbulent viscoplastic fluid flow on axisymmetric abrupt contraction, Fluid Dyn. Res. 53 (5) (2021) 055501, http://dx.doi.org/10.1088/1873-7005/ac2481, URL http://dx.doi.org/10.1088/1873-7005/ac2481.

[36] Pengfei Shi, Haibao Hu, Jun Wen, Hailang Sun, Luo Xie, Experimental investigation on drag reduction in turbulent pipe flow with polymer injection, J. Non-Newton. Fluid Mech. (ISSN: 0377-0257) 341 (2025) 105434, http://dx.doi.org/10.1016/j.jnnfm.2025.105434, URL https://www.sciencedirect.com/science/article/pii/S0377025725000539.

[37] David E.S. Breakey, Rouholluh Shokri, Sina Ghaemi, David S. Nobes, R. Sean Sanders, A parametric study of turbulence modulation in high-Reynolds-number, particle-laden flow in a vertical pipe, Int. J. Multiph. Flow (ISSN: 0301-9322) 194 (2026) 105414, http://dx.doi.org/10.1016/j.ijmultiphaseflow.2025.105414, URL https://www.sciencedirect.com/science/article/pii/S0301932225002897.

[38] Sébastien Wiederseiner, Nicolas Andreini, Gaël Epely-Chauvin, Christophe Ancey, Refractive-index and density matching in concentrated particle suspensions: a review, Exp. Fluids 50 (2011) 1183–1206, http://dx.doi.org/10.1007/s00348-010-0996-8.

[39] Hideki Murakawa, Michitsugu Mori, Yasushi Takeda, Ultrasonic Doppler method, in: Yasushi Takeda (Ed.), Ultrasonic Doppler Velocity Profiler for Fluid Flow, Springer Japan, Tokyo, 2012, pp. 43–69, http://dx.doi.org/10.1007/978-4-431-54026-7_3.

[40] Christian Poelma, Ultrasound imaging velocimetry: a review, Exp. Fluids 58 (2017) 1–28, http://dx.doi.org/10.1007/s00348-016-2283-9.

[41] Johan Wiklund, Mats Stading, A. Pettersson, Anders Rasmuson, A comparative study of UVP and LDA techniques for highly concentrated pulp fibre suspensions in pipe flow, AIChE J. 52 (2006) 484–495, http://dx.doi.org/10.1002/aic.10653.

[42] Johan Wiklund, Mattias Johansson, Jeelani Shaik, Peter Fischer, Erich Windhab, Mats Stading, Anne-Marie Hermansson, et al., In-line ultrasound based rheometry of industrial and model suspensions flowing through pipes, in: Third International Symposium on Ultrasonic Doppler Methods for Fluid Engineering. Lausanne: EFPL, 2002.

[43] Johan Wiklund, Beat Birkhofer, Shaik AK Jeelani, Mats T Stading, Erich J Windhab, In-line rheometry of particulate suspensions by pulsed ultrasound velocimetry combined with pressure difference method, Appl. Rheol. 22 (4) (2012) 42232, http://dx.doi.org/10.3933/ApplRheol-22-42232.

[44] Reinhardt Kotze, Rainer Haldenwang, Paul Slatter, Rheological characterization of highly concentrated mineral suspensions using ultrasound velocity profiling with combined pressure difference method, Appl. Rheol. 18 (2019) http://dx.doi.org/10.1515/arh-2008-0020, 62114–1.

[45] Takahisa Shiratori, Yuji Tasaka, Yuichi Murai, Rapid rheological characterization of a viscoelastic fluid based on spatiotemporal flow velocimetry, Exp. Therm. Fluid Sci. (ISSN: 0894-1777) 71 (2016) 1–13, http://dx.doi.org/10.1016/j.expthermflusci.2015.10.012.

[46] Reinhardt Kotze, Rainer Haldenwang, Veruscha Fester, Werner Rössle, In-line rheological characterisation of wastewater sludges using non-invasive ultrasound sensor technology, Water SA 41 (5) (2015) 683–690, http://dx.doi.org/10.4314/wsa.v41i5.11.

[47] Serish Tanya Hussain, Jeffrey Peakall, Martyn Barnes, Timothy Hunter, Simultaneous velocity and concentration profiling of nuclear waste suspensions in pipe-flow, using ultrasonic Doppler and backscatter analysis, in: Proceedings of Meetings on Acoustics, 45, (1) AIP Publishing, 2021, http://dx.doi.org/10.1121/2.0001525.

[48] Said Alhaddad, Robert Jan Labeur, Wim Uijttewaal, Large-scale experiments on breaching flow slides and the associated turbidity current, J. Geophys. Res.: Earth Surf. 125 (10) (2020) http://dx.doi.org/10.1029/2020JF005582, e2020JF005582.

[49] Sanehiro Wada, Hiroshige Kikura, Masanori Aritomi, Michitsugu Mori, Yasushi Takeda, Development of pulse ultrasonic Doppler method for flow rate measurement in power plant multilines flow rate measurement on metal pipe, J. Nucl. Sci. Technol. 41 (3) (2004) 339–346, http://dx.doi.org/10.1080/18811248.2004.9715493.

[50] Sanehiro Wada, Takahide Endo, Kenichi Tezuka, Noriyuki Furuichi, Experimental study on large flow rate monitoring downstream of double elbows using an ultrasonic velocity profile method, J. Power Energy Syst. 6 (3) (2012) 435–445, http://dx.doi.org/10.1299/jpes.6.435.

[51] Yuichi Murai, Yuji Tasaka, Yasushi Takeda, Time-resolved flowmetering of gas-liquid two-phase pipe flow by ultrasound pulse Doppler method, in: AIP Conference Proceedings, 1428, (1) American Institute of Physics, (ISSN: 0094-243X) 2012, pp. 311–318, http://dx.doi.org/10.1063/1.3694720.

[52] Noriyuki Furuichi, Fundamental uncertainty analysis of flowrate measurement using the ultrasonic Doppler velocity profile method, Flow Meas. Instrum. 33 (2013) 202–211, http://dx.doi.org/10.1016/j.flowmeasinst.2013.07.004.

[53] David H Evans, Jørgen Arendt Jensen, Michael Bachmann Nielsen, Ultrasonic colour Doppler imaging, Interface Focus. 1 (4) (2011) 490–502, http://dx.doi.org/10.1098/rsfs.2011.0017.

[54] F Ein-Mozaffari, CPJ Bennington, GA Dumont, D Buckingham, Measuring flow velocity in pulp suspension mixing using ultrasonic Doppler velocimetry, Chem. Eng. Res. Des. 85 (5) (2007) 591–597, http://dx.doi.org/10.1205/cherd06143.

[55] Reinhardt Kotze, Johan Wiklund, Rainer Haldenwang, Optimisation of pulsed ultrasonic velocimetry system and transducer technology for industrial applications, Ultrasonics (ISSN: 0041-624X) 53 (2) (2013) 459–469, http://dx.doi.org/10.1016/j.ultras.2012.08.014.

[56] Abdelhakim Benslimane, Bekkour Karim, Pierre François, Hocine Bechir, Laminar and turbulent pipe flow of bentonite suspensions, J. Pet. Sci. Eng. 139 (2015) 85–93, http://dx.doi.org/10.1016/j.petrol.2015.12.020.

[57] B.E. Launder, D.B. Spalding, The numerical computation of turbulent flows, Comput. Methods Appl. Mech. Engrg. (ISSN: 00457825) 3 (2) (1974) http://dx.doi.org/10.1016/0045-7825(74)90029-2.

[58] Dhruv Mehta, Adithya Krishnan Thota Radhakrishnan, Jules van Lier, Francois Clemens, A wall boundary condition for the simulation of a turbulent non-Newtonian domestic slurry in pipes, Water (Switzerland) (ISSN: 20734441) 10 (2) (2018) http://dx.doi.org/10.3390/w10020124.

[59] Dhruv Mehta, Adithya Krishnan Thota Radhakrishnan, Jules van Lier, Francois Clemens, Sensitivity analysis of a wall boundary condition for the turbulent pipe flow of Herschel-Bulkley fluids, Water (Switzerland) (ISSN: 20734441) 11 (1) (2018) http://dx.doi.org/10.3390/w11010019.

[60] F. Durst, J. Jovanović, J. Sender, LDA measurements in the near-wall region of a turbulent pipe flow, J. Fluid Mech. 295 (1995) 305–335, http://dx.doi.org/10.1017/S0022112095001984.

[61] Adithya Krishnan Thota Radhakrishnan, Christian Poelma, Jules van Lier, Francois Clemens, Laminar-turbulent transition of a non-Newtonian fluid flow, J. Hydraul. Res. (ISSN: 00221686) 59 (2) (2021) http://dx.doi.org/10.1080/00221686.2020.1770876.

[62] A.C.J. de Korte, H.J.H. Brouwers, Ultrasonic sound speed analysis of hydrating calcium sulphate hemihydrate, J. Mater. Sci. 46 (21) (2011) 7228–7239, http://dx.doi.org/10.1007/s10853-011-5682-6, URL http://dx.doi.org/10.1007/s10853-011-5682-6.

[63] Krishnan Thota Radhakrishnan, A. Poelma, J. van Lier, F. Clemens, Laminar-turbulent transition of a non-Newtonian fluid flow, J. Hydraul. Res. 59 (2) (2020) 235–249, http://dx.doi.org/10.1080/00221686.2020.1770876, URL http://dx.doi.org/10.1080/00221686.2020.1770876.

[64] Anirban Chaudhuri, Norman M. Wereley, Sanjay Kotha, Ramachandran Radhakrishnan, Tirumalai S. Sudarshan, Viscometric characterization of cobalt nanoparticle-based magnetorheological fluids using genetic algorithms, J. Magn. Magn. Mater. (ISSN: 0304-8853) 293 (1) (2005) 206–214, http://dx.doi.org/10.1016/j.jmmm.2005.01.061, URL https://www.sciencedirect.com/science/article/pii/S0304885305001587.

[65] Winslow H. Herschel, Ronald Bulkley, Konsistenzmessungen von Gummi-Benzollösungen, Kolloid-Zeitschrift (ISSN: 0303402X) 39 (4) (1926) http://dx.doi.org/10.1007/BF01432034.

[66] J.C. Baudez, F. Markis, N. Eshtiaghi, P. Slatter, The rheological behaviour of anaerobic digested sludge, Water Res. (ISSN: 0043-1354) 45 (17) (2011) 5675–5680, http://dx.doi.org/10.1016/j.watres.2011.08.035, URL https://www.sciencedirect.com/science/article/pii/S0043135411004830.

[67] Flora Markis, Jean-Christophe Baudez, Rajarathinam Parthasarathy, Paul Slatter, Nicky Eshtiaghi, Rheological characterisation of primary and secondary sludge: Impact of solids concentration, Chem. Eng. J. (ISSN: 1385-8947) 253 (2014) 526–537, http://dx.doi.org/10.1016/j.cej.2014.05.085, URL https://www.sciencedirect.com/science/article/pii/S1385894714006603.

[68] E. Farno, K. Coventry, P. Slatter, N. Eshtiaghi, Role of regression analysis and variation of rheological data in calculation of pressure drop for sludge pipelines, Water Res. (ISSN: 0043-1354) 137 (2018) 1–8, http://dx.doi.org/10.1016/j.watres.2018.02.059, URL https://www.sciencedirect.com/science/article/pii/S0043135418301726.

[69] S. Benhadid, G. Maurice, R. Devienne, M. Lebouche, M. Lucius, Caractéristiques rhéologiques, coéfficient de frottement et écoulement en situation réelle de fluides à seuil, Rheol. Acta 27 (6) (1988) 628–633, http://dx.doi.org/10.1007/BF01337458, URL http://dx.doi.org/10.1007/BF01337458.

[70] Nicky Eshtiaghi, Flora Markis, Shao Dong Yap, Jean-Christophe Baudez, Paul Slatter, Rheological characterisation of municipal sludge: A review, Water Res. (ISSN: 0043-1354) 47 (15) (2013) 5493–5510, http://dx.doi.org/10.1016/j.watres.2013.07.001, URL https://www.sciencedirect.com/science/article/pii/S0043135413005629.

[71] A.K. Thota Radhakrishnan, J.B. van Lier, F.H.L.R. Clemens, Rheological characterisation of concentrated domestic slurry, Water Res. (ISSN: 0043-1354) 141 (2018) 235–250, http://dx.doi.org/10.1016/j.watres.2018.04.064, URL https://www.sciencedirect.com/science/article/pii/S0043135418303580.

[72] R.M. Turian, T.W. Ma, F.L.G. Hsu, D.J. Sung, Characterization, settling, and rheology of concentrated fine particulate mineral slurries, Powder Technol. (ISSN: 0032-5910) 93 (3) (1997) 219–233, http://dx.doi.org/10.1016/S0032-5910(97)03274-9, URL https://www.sciencedirect.com/science/article/pii/S0032591097032749.

[73] Yang Mu, Han-Qing Yu, Rheological and fractal characteristics of granular sludge in an upflow anaerobic reactor, Water Res. (ISSN: 0043-1354) 40 (19) (2006) 3596–3602, http://dx.doi.org/10.1016/j.watres.2006.05.041, URL https://www.sciencedirect.com/science/article/pii/S0043135406003241.

[74] A.K. Thota Radhakrishnan, J.B. van Lier, F. H.L.R. Clemens, Rheological characterisation of concentrated domestic slurry, Water Res. (ISSN: 18792448) 141 (2018) http://dx.doi.org/10.1016/j.watres.2018.04.064.

[75] A.K. Thota Radhakrishnan, Domestic Slurry Hydraulics in Transport, TU Delft, (Ph.D. thesis), 2019.

[76] R. Rooki, F.D. Ardejani, A. Moradzadeh, et al., Optimal determination of rheological parameters for Herschel-Bulkley drilling fluids using genetic algorithms (GAs), Korea-Australia Rheol. J. 24 (2012) 163–170, http://dx.doi.org/10.1007/s13367-012-0020-3, URL http://dx.doi.org/10.1007/s13367-012-0020-3.

[77] G. Chauhan, A. Verma, A. Das, et al., Rheological studies and optimization of Herschel-Bulkley flow parameters of viscous karaya polymer suspensions using GA and PSO algorithms, Rheol. Acta 57 (2018) 267–285, http://dx.doi.org/10.1007/s00397-017-1060-x, URL http://dx.doi.org/10.1007/s00397-017-1060-x.

[78] R.M. Clapp, Turbulent heat transfer in pseudoplastic non-Newtonian fluids, in: International Developments in Heat Transfer, ASME Part III, Section a, 1961, p. 652.

[79] Richard A. Chilton, Richard Stainsby, Pressure loss equations for laminar and turbulent non-Newtonian pipe flow, J. Hydraul. Eng. (ISSN: 0733-9429) 124 (5) (1998) http://dx.doi.org/10.1061/(asce)0733-9429(1998)124:5(522).

[80] M. Rudman, H.M. Blackburn, L.J.W. Graham, L. Pullum, Turbulent pipe flow of shear-thinning fluids, J. Non-Newton. Fluid Mech. (ISSN: 03770257) 118 (1) (2004) http://dx.doi.org/10.1016/j.jnnfm.2004.02.006.

[81] Richard P. Brent, Algorithms for Minimization Without Derivatives, Courier Corporation, 2013.

[82] Felipe O. Basso, Admilson T. Franco, Diogo B. Pitz, Large-eddy simulation of turbulent pipe flow of Herschel-Bulkley fluids-assessing subgrid-scale models, Comput. & Fluids 244 (2022) 105522.

[83] M.R. Malin, Turbulent pipe flow of Herschel-Bulkley fluids, Int. Commun. Heat Mass Transfer (ISSN: 07351933) 25 (3) (1998) http://dx.doi.org/10.1016/S0735-1933(98)00019-0.

[84] D.O.A. Cruz, F.T. Pinho, Turbulent pipe flow predictions with a low Reynolds number k-ϵ model for drag reducing fluids, J. Non-Newton. Fluid Mech. (ISSN: 03770257) 114 (2–3) (2003) http://dx.doi.org/10.1016/S0377-0257(03)00119-8.

[85] J. Nikuradse, Gesetzmäßigkeiten der turbulenten Strömung in glatten Rohren (Nachtrag), Forsch. Auf Dem Geb. Des Ingenieurwesens (ISSN: 0015-7899) 4 (1) (1933) http://dx.doi.org/10.1007/BF02716946, 44–44.

[86] B. Rabinowitsch, Über die Viskosität und Elastizität von Solen, Z. Für Phys. Chem. (ISSN: 0942-9352) 145A (1) (1929) http://dx.doi.org/10.1515/zpch-1929-14502.

[87] Melvin Mooney, Explicit Formulas for Slip and Fluidity, J. Rheol. (ISSN: 0097-0360) 2 (2) (1931) http://dx.doi.org/10.1122/1.2116364.

[88] R.P. Chhabra, J.F. Richardson, Non-newtonian flow and applied rheology, Non-Newtonian Flow and Applied Rheology, 2008, http://dx.doi.org/10.1016/B978-0-7506-8532-0.X0001-7.

[89] Arturo A. Arosemena, Ronnie Andersson, Helge I. Andersson, Jannike Solsvik, Effects of shear-thinning rheology on near-wall turbulent structures, J. Fluid Mech. 925 (2021) A37, http://dx.doi.org/10.1017/jfm.2021.657.

[90] J. Singh, M. Rudman, H.M. Blackburn, Reynolds number effects in pipe flow turbulence of generalized Newtonian fluids, Phys. Rev. Fluids (ISSN: 2469990X) 3 (9) (2018) http://dx.doi.org/10.1103/PhysRevFluids.3.094607.

[91] S. Lovato, A. Kirichek, S.L. Toxopeus, J.W. Settels, G.H. Keetels, Validation of the resistance of a plate moving through mud: CFD modelling and towing tank experiments, Ocean Eng. (ISSN: 0029-8018) 258 (2022) 111632, http://dx.doi.org/10.1016/j.oceaneng.2022.111632, URL https://www.sciencedirect.com/science/article/pii/S0029801822009933.

[92] Noman Yousuf, Daniel Lester, Murray Rudman, Marco Dentz, Nicky Eshtiaghi, Turbulent pipe flow of thixotropic fluids, J. Fluid Mech. 1011 (2025) A45, http://dx.doi.org/10.1017/jfm.2025.376.

[93] Julia Claesson, Anders Rasmuson, Johan Wiklund, Tomas Wikström, Measurement and analysis of flow of concentrated fiber suspensions through a 2-D sudden expansion using UVP, AIChE J. 59 (3) (2013) 1012–1021, http://dx.doi.org/10.1002/aic.13881.

[94] Jagmohan Singh, Murray Rudman, H.M. Blackburn, Andrew Chryss, Lionel Pullum, L. Graham, The importance of rheology characterization in predicting turbulent pipe flow of generalized Newtonian fluids, J. Non-Newton. Fluid Mech. 232 (2016) 11–21, http://dx.doi.org/10.1016/j.jnnfm.2016.03.013.